14th AIAA/CEAS Aeroacoustics Conference
(29th AIAA Aeroacoustics Con
5 - 7 May 2008, Vancouver, British Columbia Canada

AIAA 2008-3049

A high-order algorithm for compressible LES in CAA applications

F. Daude*, T. Emmert, P. Lafon†
LaMSID, UMR EDF/CNRS 2832, Clamart, France

F. Crouzet‡
EDF R&D, Department of Applied Mechanics and Acoustics, Clamart, France

and C. Bailly§
LMFA, ECL & UMR CNRS 5509, Ecully, France

A high-order finite-difference algorithm is proposed in the aim of LES and CAA applications. The subgrid scale dissipation is performed by the explicit high-order numerical filter used for numerical stability purpose. A shock-capturing non-linear filter is also implemented to deal with compressible discontinuous flows. In order to tackle complex geometries, an overset-grid approach is used. High-order interpolations make it possible to ensure the communication between overlapping domains. The whole algorithm is first validated on canonical flow problems to illustrate both its properties for shock-capturing as well as for accurate wave propagation. Then, the influence of the multi-domain approach on the high-order spatial accuracy is assessed. Afterwards, the algorithm is extended to dynamic mesh applications with overlapping grids. Finally, two industrial cases are presented to highlight the potential of the proposed algorithm.

I. Introduction

In a wide range of technical fields such as aircrafts, automotive engineering, trains, turbomachinery, power plants, non-linear interactions between the turbulent flow and the acoustic fields produce undesirable high pressure levels.[1] They are the source of noise pollution which is a major environmental issue. The radiated noise can also induce vibrations and damages. This is particularly the case in confined flows. In addition, turbulent flows or acoustic waves can couple with moving structures involving fluid/structure interaction. The calculation of both the unsteady flow and the associated sound must be performed in the same computation. This is referred as Direct Noise Computation (DNC) in the literature.[2] Using DNC is an efficient way to identify the fluid mechanism contributing to the sound production and therefore, a useful tool to reduce the noise radiation. The feasibility of DNC is now demonstrated in the literature via Direct Numerical Simulation (DNS)[3–5] and Large-Eddy Simulation (LES).[6–8]

Application of compressible LES to computational aeroacoustics (CAA) problems makes it possible to tackle applications with industrial or practical relevance. The large disparity in the characteristic scales of the acoustic and the flow fluctuations, and the need to accurately resolve high wavenumber fluctuations require the use of numerical methods with minimal dissipation and dispersion errors.[1] In this context, the Dispersion-Relation-Preserving (DRP)[9] or optimized[10] high-order finite-difference schemes in conjunction with selective filter are an attractive choice for LES to reduce both amplitude and phase numerical errors. Transonic compressible turbulent flows are characterized by the presence of shock waves which interact with turbulence. A shock-capturing scheme must also be implemented but implies the introduction of numerical

*Post-Doc Position.
†Research engineer, AIAA Senior Member.
‡Research engineer.
§Professor at Ecole Centrale de Lyon & Institut Universitaire de France, AIAA Senior Member.

dissipation. The development of numerical algorithms that capture discontinuities and also resolve both the scales of turbulence and the generated acoustic waves in compressible turbulent flows remains thus a significant challenge. In order to treat industrial configurations, a new numerical code called SAFARI (Simulation of Aeroacoustic Flows And Resonance and Interaction) has been developed. To address complex geometrical configurations, overset-grid strategy is used with high-order interpolation for the communication between non-coincident grids.[11–13]

This paper is organized as follows. After briefly presented the governing equations in Section II, the proposed algorithm is presented in Section III. This algorithm is based on optimized high-order finite-difference schemes in conjunction with optimized high-order low-pass spatial filters.[10] To highlight the spectral behavior of our proposed algorithm, a linear analysis is performed on the global numerical method including both spatial, temporal discretizations and selective filter. The shock-capturing procedure is performed via a non-linear filter after the time integration. A special attention is paid on the shock-detector which is the key issue in the preservation of the algorithm spectral behavior. In order to tackle complex geometries as multiple bodies, the employed overset-grid strategy with high-order Lagrangian interpolation is presented in Section IV where a linear analysis of the interpolation error is assessed. The ability of the present algorithm to capture discontinuities in canonical 1-D and 2-D problems without damaging its initial propagation properties is discussed in Section V. Afterwards, it is shown that the multi-domain strategy does not corrupt the algorithm characteristics via numerical examples. Then, in Section VI, the high-order scheme is extended to moving overset grids. The time metric error cancellation which is required to ensure the free-stream preservation and the stability criterion linked to the mesh displacement are discussed. Finally, two realistic cases are briefly presented in Section VII with complex physical flow/acoustics coupling in real geometries to highlight the potential of the present solver.

II. Governing equations

A. Fluid dynamics

The three-dimensional Navier-Stokes equations are expressed in Cartesian coordinates for a viscous compressible Newtonian fluid. After the application of a general time-dependant curvilinear transformation $(x, y, z, t) \rightarrow (\xi, \eta, \zeta, \tau)$,[14,15] these equations are written in the following strong conservative form:

$$\partial_\tau Q + \partial_\xi \Big(E - E^\nu \Big) + \partial_\eta \Big(F - F^\nu \Big) + \partial_\zeta \Big(G - G^\nu \Big) = 0. \tag{1}$$

with $Q = U/J$ where $U = (\rho, \rho u, \rho v, \rho w, \rho e)$ is the vector of conservative variables, ρ is the density, u, v and w are the Cartesian velocity components of the vector $\vec{V}$, e is the total specific energy:

$$\rho e = \frac{p}{\gamma - 1} + \frac{1}{2}\rho \left(u^2 + v^2 + w^2 \right),$$

where p is the pressure, γ the specific heat ratio and J the Jacobian of the coordinate transformation $(x, y, z) \rightarrow (\xi, \eta, \zeta)$. E, F and G are the inviscid flux-vectors which can be expressed as:

$$E = \xi_t Q + \frac{1}{J} \begin{pmatrix} \rho\Theta_\xi \\ \rho u\Theta_\xi + p\xi_x \\ \rho v\Theta_\xi + p\xi_y \\ \rho w\Theta_\xi + p\xi_z \\ (\rho e + p)\,\Theta_\xi \end{pmatrix}, \quad F = \eta_t Q + \frac{1}{J} \begin{pmatrix} \rho\Theta_\eta \\ \rho u\Theta_\eta + p\eta_x \\ \rho v\Theta_\eta + p\eta_y \\ \rho w\Theta_\eta + p\eta_z \\ (\rho e + p)\,\Theta_\eta \end{pmatrix}, \quad G = \zeta_t Q + \frac{1}{J} \begin{pmatrix} \rho\Theta_\zeta \\ \rho u\Theta_\zeta + p\zeta_x \\ \rho v\Theta_\zeta + p\zeta_y \\ \rho w\Theta_\zeta + p\zeta_z \\ (\rho e + p)\,\Theta_\zeta \end{pmatrix}.$$

The contra-variant velocity components Θ_ξ, Θ_η and Θ_ζ are defined as:

$$\Theta_\xi = u\xi_x + v\xi_y + w\xi_z, \quad \Theta_\eta = u\eta_x + v\eta_y + w\eta_z \quad \text{and} \quad \Theta_\zeta = u\zeta_x + v\zeta_y + w\zeta_z.$$

The quantities ξ_t, η_t and ζ_t are the time metrics; $\xi_x, \xi_y, \xi_z, \eta_x, \eta_y, \eta_z, \zeta_x, \zeta_y$ and ζ_z designate the spatial metrics. The subscripts denote the partial derivatives. E^ν, F^ν and G^ν are the viscous flux-vectors. Their expression are the same as in the case of time-invariant generalized coordinates.[16,17]

B. Geometrical conservation

With the strong-conservation form in Equation (1), the following relations must be satisfied numerically to ensure free-stream preservation when a finite-difference discretization is used:[18]

$$\begin{cases} \left(\frac{1}{J}\xi_x\right)_\xi + \left(\frac{1}{J}\eta_x\right)_\eta + \left(\frac{1}{J}\zeta_x\right)_\zeta = 0 \\ \left(\frac{1}{J}\xi_y\right)_\xi + \left(\frac{1}{J}\eta_y\right)_\eta + \left(\frac{1}{J}\zeta_y\right)_\zeta = 0 \\ \left(\frac{1}{J}\xi_z\right)_\xi + \left(\frac{1}{J}\eta_z\right)_\eta + \left(\frac{1}{J}\zeta_z\right)_\zeta = 0 \\ \left(\frac{1}{J}\right)_\tau + \left(\frac{1}{J}\xi_t\right)_\xi + \left(\frac{1}{J}\eta_t\right)_\eta + \left(\frac{1}{J}\zeta_t\right)_\zeta = 0 \end{cases} \tag{2}$$

The last relation only concerns time-dependent meshes and is called the geometric conservation law (GCL).[19] In order to satisfy the numerical metric error cancellation and to ensure the free-stream preservation, the spatial metrics are expressed in the conservative form proposed by Thomas and Lombard:[19]

$$\begin{cases} \frac{1}{J}\xi_x = (y_\eta z)_\zeta - (y_\zeta z)_\eta \\ \frac{1}{J}\xi_x = (y_\zeta z)_\xi - (y_\xi z)_\zeta \\ \frac{1}{J}\xi_x = (y_\xi z)_\zeta - (y_\eta z)_\xi \end{cases} \tag{3}$$

Time metrics are used for moving/deforming grid computations. Their expression are given in Section VI.

III. Numerical method

A. Spatial discretization

First derivatives at interior grid points are determined using the optimized 11-point centered finite-difference scheme proposed by Bogey and Bailly:[10]

$$\partial_\xi E_{i,j,k} \approx \frac{1}{\Delta\xi}\sum_{m=1}^{5} s_m\Big(E_{i+m,j,k} - E_{i-m,j,k}\Big). \tag{4}$$

This non-dissipative scheme is optimized in the wavenumber space to reduce the dispersion error following the idea of Tam and Webb.[9] The linear analysis shows that this scheme is able to resolve accurately perturbations with only four points per wavelength such as shown in Figure 1 (a). The same scheme has been applied successfully[7,8] for the direct computation of jet noise using LES. The coefficients s_m are given in Appendix A.

B. Temporal integration

The spatial discretization step leads to a semi-discrete form as:

$$\frac{\mathrm{d}Q_{i,j,k}}{\mathrm{d}\tau} + R_{i,j,k} = 0 \tag{5}$$

with $R_{i,j,k}$ the residual of the discretized inviscid and viscous terms. Equation (5) can be solved by both explicit and implicit time integration methods. In the present work, the equations are integrated in time with the classical explicit four-stage Runge-Kutta scheme (RK4) :

$$Q^{(l)}_{i,j,k} = Q^{n}_{i,j,k} - \Delta\tau\beta^{(l)}R^{(l-1)}_{i,j,k} \quad \forall l \in \{1,...,4\} \tag{6}$$

with $Q^{(0)} = Q^n$. The damping and stability properties of the RK4 scheme obtained with the linear analysis are shown in Figure 1 (c).

C. Low-pass filter

After the application of the Runge-Kutta scheme, the explicit optimized 11-point spatial low-pass filter proposed by Bogey and Bailly[10] is used to remove spurious high-frequency spatial oscillations:

$$W^{(5)}_{i,j,k} = W^{(4)}_{i,j,k} - \sigma_f \left[F^{\xi}\left(W^{(4)}_{i,j,k}\right) + F^{\eta}\left(W^{(4)}_{i,j,k}\right) + F^{\zeta}\left(W^{(4)}_{i,j,k}\right)\right] \tag{7}$$

where

$$F^{\xi}\left(W^{(4)}_{i,j,k}\right) = d_0 W^{(4)}_{i,j,k} + \sum_{m=1}^{5} d_m \left(W^{(4)}_{i+m,j,k} + W^{(4)}_{i-m,j,k}\right)$$

with $0 \leq \sigma_f \leq 1$ for the filtering strength ; and $W = (\rho, \rho u, \rho v, \rho w, p)^T$.

This filter is optimized in the wavenumber space: the linear analysis shows that this filter only damps the perturbations not accurately resolved by the spatial scheme of Equation (4) as shown in Figure 1 (b). The coefficients d_m are given in Appendix A.

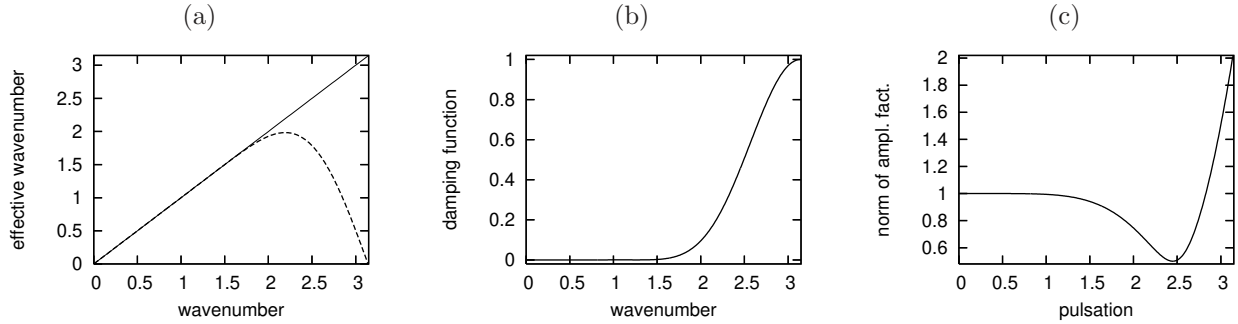

Figure 1. (a) Comparison between the exact – and the effective - - wavenumber of the spatial discretization; (b) Damping function of the selective filter as a function of the wavenumber $k\Delta x$; (c) Dissipative characteristic of the RK4 scheme as a function of the pulsation $\omega\Delta t$.

D. Linear Analysis

The Von Neumann method is used to analyze the damping and dispersive properties of the algorithm presented previously. This analysis is only applied on linear equations with periodic boundary conditions. For non-linear equations, the results obtained with the linear analysis are not sufficient. However, linear stability is a necessary condition for non-linear problems.[20]

The Von Neumann method is applied to the global algorithm (spatial, temporal discretizations and low-pass filter) for the following linear advection equation:

$$\partial_t u + a\partial_x u = 0 \tag{8}$$

The algorithm can be decomposed into three steps as:

$$\begin{cases} R_i(u) = \dfrac{a}{\Delta x}\displaystyle\sum_{m=1}^{5} s_m(u_{i+m} - u_{i-m}) & \text{(spatial discretization)} \\ u_i^{(l)} = u_i^n - \Delta t \beta^{(l)} R_i(u^{(l-1)}) \qquad \forall l \in \{1, ..., 4\} & \text{(time discretization)} \\ u_i^{n+1} = u_i^{(4)} - \sigma_f \left[d_0 u_i^{(4)} + \displaystyle\sum_{m=1}^{5} d_m \left(u_{i+m}^{(4)} + u_{i-m}^{(4)}\right)\right] & \text{(low-pass filter)} \end{cases}$$

with $u_i^{(0)} = u_i^n$.

The Von Neumann method is based on the Fourier transform. We consider a single harmonic $u_i^n = \hat{u}^n e^{Iik\Delta x}$ with $\hat{u}^n$ the amplitude, $k\Delta x$ the phase angle corresponding to the wavenumber k and $I^2 = -1$. In order to evaluate the algorithm amplification factor defined as $g = \hat{u}^{n+1}/\hat{u}^n$, the Fourier transform is applied to the three stages of the computation:

$$\begin{cases} \hat{R}(u) = I\dfrac{a}{\Delta x}\hat{u}k^*\Delta x & \text{with} \quad k^*\Delta x = 2\displaystyle\sum_{m=1}^{5} s_m \sin(mk\Delta x) \qquad \text{(spatial discret.)} \\ \hat{u}^{(4)} = \left(1 + \displaystyle\sum_{l=1}^{4} \gamma_l(-\Delta t I \frac{a}{\Delta x}k^*\Delta x)^l\right)\hat{u}^n & \text{with} \quad \gamma_l = \displaystyle\prod_{q=4-l+1}^{4} \beta^{(q)} \qquad \text{(time discret.)} \\ \hat{u}^{n+1} = (1 - \sigma_f \hat{D})\hat{u}^{(4)} & \text{with} \quad \hat{D} = d_0 + 2\displaystyle\sum_{m=1}^{5} d_m \cos(mk\Delta x) \quad \text{(low-pass filter)} \end{cases}$$

Finally, the amplification factor of the global algorithm can be written as:

$$g = (1 - \sigma_d \hat{D})\left(1 + \sum_{l=1}^{4} \gamma_l(-I\sigma k^*\Delta x)^l\right) \tag{9}$$

with the CFL number $\sigma = \dfrac{a\Delta t}{\Delta x}$.

The amplification factor g which can be rewritten as $g = |g|e^{I\phi}$ is now compared with the exact factor: $g_{\text{ex}} = e^{-I\sigma k\Delta x}$. The algorithm damping property is given by the norm $|g|$ and the dispersive one by the relative phase error: $\phi + \sigma k\Delta x$. The results with $\mathsf{CFL} = 1$ and $\sigma_f = 0.2$ are displayed in Figure 2. With

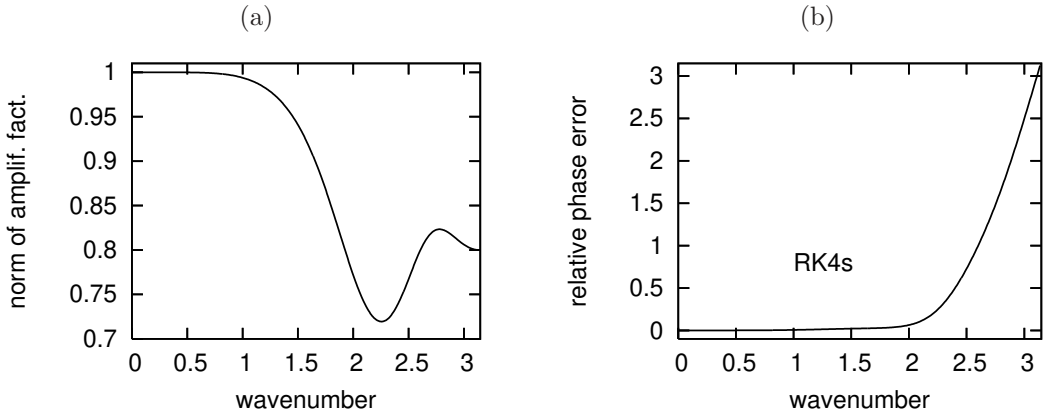

Figure 2. Damping and dispersion errors as a function of the wavenumber $k\Delta x$: (a) Norm of the amplification factor $|g|$; (b) relative phase error $\phi + \sigma k\Delta x$.

respect to the damping character of the spatial scheme and the linear filter presented in Figure 1, by taking $\mathsf{CFL} = 1$, the explicit time integration damages the upper bound of the range of well-resolved wavenumber: $k\Delta x \leq \pi/2$. To known quantitatively the accuracy domain of the global algorithm, an accuracy limit is estimated from the following arbitrary criterion:

$$|1 - \mathcal{H}| \leq 5 \times 10^{-4} \tag{10}$$

with the ratio $\mathcal{H} = g/g_{\text{ex}}$. The accuracy domain of the global algorithm is thus reduced to $0 \leq k\Delta x \leq 0.65$, that is to say in term of number of points per wavelength: $\lambda_a/\Delta x \approx 9.66$.

E. LES strategy

The LES strategy used in the present work is the same as the one employed by Bogey and Bailly[7,8] and by Rizzetta *et al.*[21] The compressible LES formalism of Vreman[22] is retained to express the filtered equations in conservative form. The selective filter used to improve the numerical stability of the centered non-dissipative spatial discretization is also employed to separate the large scales from the small ones. In addition, this linear filter takes into account the dissipative effects of the subgrid scales by draining energy at the cut-off frequency. Indeed, the selective filter leaves flow features larger than the cut-off wavelengths unaffected, while properly removing the energy being transferred to smaller wave lengths. In addition, the interactions between the resolved and the unresolved scales are neglected. Thus, no additional explicit subgrid scale model is used.

F. Shock-capturing procedure

1. *Adaptive shock-capturing filter*

A shock-capturing filter[23] is applied on the conservative variables after the use of the selective filter in Equation (7). This non-linear filter is based on the artificial dissipation model proposed by Kim and Lee.[24] The same model has been recently used in[25] for choked nozzles and supersonic diffusers. However, in the present work, only the low-order shock-capturing term of the model of Kim and Lee is applied. Following Yee *et al.*,[26] the dissipative part of the shock-capturing procedure is applied after the time integration process as a non-linear filter:

$$Q_{i,j,k}^{n+1} = Q_{i,j,k}^{(5)} + \Delta t \left(D_{i,j,k}^{\xi} + D_{i,j,k}^{\eta} + D_{i,j,k}^{\zeta} \right), \tag{11}$$

where the dissipative part of the shock-capturing procedure in the ξ-direction can be expressed as:

$$D_{i,j,k}^{\xi} = \frac{1}{\Delta\xi} \left(\mathcal{D}_{i+1/2} - \mathcal{D}_{i-1/2} \right),$$

where $\mathcal{D}_{i+1/2}$ is the dissipative numerical flux of the filtering operator:

$$\mathcal{D}_{i+1/2} = \frac{\Delta|\lambda|_{i+1/2}^{\xi}}{J_{i+1/2}} \epsilon_{i+1/2}^{(2)} \left(U_{i+1,j,k}^{(5)} - U_{i,j,k}^{(5)} \right). \tag{12}$$

The stencil eigenvalue $\Delta|\lambda|_{i+1/2}^{\xi}$ is defined as:

$$\Delta|\lambda|_{i+1/2}^{\xi} = \max_{m=-2}^{3} (|\lambda^{\xi}|_{i+m,j,k}) - \min_{m=-2}^{3} (|\lambda^{\xi}|_{i+m,j,k}),$$

where the eigenvalue is expressed in the time-dependant generalized coordinates:

$$\lambda^{\xi} = \xi_t + \Theta_{\xi} + c||\vec{\nabla}\xi|| \quad \text{with} \quad \vec{\nabla}\xi = (\xi_x, \xi_y, \xi_z)^T$$

and $c = \sqrt{\dfrac{\gamma p}{\rho}}$ is the sound speed. The midpoint value of the transformation Jacobian is estimated by $J_{i+1/2} = (J_i + J_{i+1})/2$. The non-linear dissipation function is expressed:

$$\epsilon_{i+1/2}^{(2)} = \kappa_{j,k} \max_{m=-2}^{3} (\nu_{i+m,j,k}^{\xi}) \quad \text{with} \quad \nu_{i,j,k}^{\xi} = \frac{|p_{i-1,j,k} - 2p_{i,j,k} + p_{i+1,j,k}|}{p_{i-1,j,k} + 2p_{i,j,k} + p_{i+1,j,k}}$$

In this expression, ν^{ξ} is the pressure shock detector proposed by Jameson *et al.*[27] Finally, the definition of the adaptive control constant $\kappa_{j,k}$ proposed by Kim and Lee[24] is retained.

According to Garnier *et al.*,[28] the classical high-order shock-capturing schemes show excessive numerical dissipation in the frame of freely decaying turbulence. Thus, a local application of the shock-capturing scheme is necessary to reduce the numerical dissipation, and the determination of the shock location is a crucial problem to minimize this excessive damping. In the filter presented here, this determination is performed via the Jameson sensor. However, in the frame of shock/turbulence interaction,[29] this sensor is

not able to distinguish turbulent fluctuations from strong gradients. Therefore, a modified Jameson sensor[23] is used in this paper. The Jameson sensor can be rewritten in the following form:

$$\nu^{\xi}_{i,j,k} = \frac{|L^{\xi}_f(p_{i,j,k})|}{p_{i,j,k} - L^{\xi}_f(p_{i,j,k})}$$

where L^{ξ}_f designates the linear second-order filter operator:

$$L^{\xi}_f(p_{i,j,k}) = -\frac{1}{4}p_{i-1,j,k} + \frac{1}{2}p_{i,j,k} - \frac{1}{4}p_{i+1,j,k}.$$

The modified sensor proposed in this work is based on the use of the optimized selective filter defined by Equation (7):

$$\begin{cases} \phi^{\xi}_{i,j,k} = \dfrac{|F^{\xi}(p_{i,j,k})|}{p_{i,j,k} - F^{\xi}(p_{i,j,k})} \\ \\ \text{with } F^{\xi}(p_{i,j,k}) = d_0 p_{i,j,k} + \displaystyle\sum_{m=1}^{5} d_m \left(p_{i+m,j,k} + p_{i-m,j,k}\right) \end{cases} \tag{13}$$

The damping feature of the two detectors is compared in 1-D, using a linear analysis. To do that, a plane wave is considered $p_i = e^{-Iki\Delta x}$ where $k\Delta x$ is the phase angle corresponding to the wavenumber k and $I^2 = -1$. We can notice on Figure 3, in contrast with the Jameson sensor, that the modified sensor does

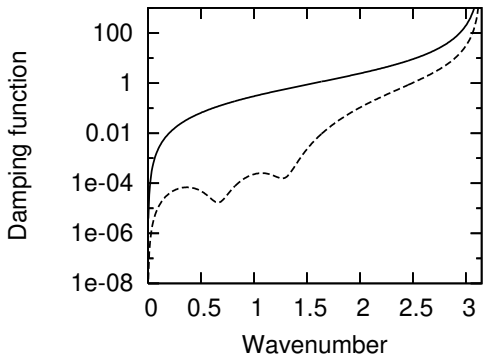

Figure 3. Damping errors of the shock detector as a function of the phase angle $k\Delta x$: – ν^{ξ}_i (classical Jameson sensor), - - ϕ^{ξ}_i (modified Jameson sensor).

not damage the low wavenumber range. However, for the high frequencies, the two detectors collapse which ensures the shock-capturing property of the scheme. In addition, theses two detectors can be used without modification in the scheme. Moreover, the computational efficiency of the algorithm is not affected by the use of the modified sensor because $F^{\xi}(p_{i,j,k})$ is already computed in the selective filtering process in Equation (7).

2. Conservative properties of the algorithm

In order to deal with shock waves, the conservative properties of the spatial scheme are studied in details. As shown in Appendix B, the 11-point centered scheme presented in Equation (4) can be recasted in a finite-volume framework which ensures its conservativity. In addition, the adaptive non-linear filter in Equation (11) is conservative due to its finite-volume definition. In Section V, the shock-capturing ability of the method proposed here is assessed.

IV. Extension to complex geometries

The high-order finite-difference algorithm satisfying conservation laws on generalized coordinates are limited to cylindrical geometries. In order to go past this limit, overset-grid techniques are used with high-

order interpolation procedure to preserve the high-order spatial accuracy.[11–13] This is addressed in the following.

A. Overset-grid strategy

In order to handle complex configurations as those including multiple bodies, the high-order algorithm presented in the previous sections is extended to general overset-grid topologies. In practice, the SAFARI code is interfaced with the freely available *Overture* library developed by the Lawrence Livermore National Laboratory.[30] The mesh including different component grids are given by *Overture*. In addition, the interpolation data such as overlapping zones, interpolation stencils and offsets are generated with *Overture*.

B. High-order interpolation

In the overset-grid approach, points of the different overlapping regions are non coincident. Therefore, the communication between overlapping component grids is performed with high-order interpolation. Following Sherer and Scott,[12] high-order explicit non-optimized Lagrangian polynomials are used to perform the interpolation stage. The interpolation process is performed in the computational domain (ξ, η, ζ, τ) as in Figure 4. The evaluation of the variable ϕ at the point P is performed via the interpolation of ϕ at P as:

$$\phi_P \approx \sum_{i=0}^{M_\xi - 1} \sum_{j=0}^{M_\eta - 1} L_i^\xi L_j^\eta \phi_{I_Q+i, J_Q+j}. \tag{14}$$

where M_ξ and M_η are the interpolation stencil length in the ξ- and η-direction respectively. Q is the first donor point of the interpolation stencil (in green in Figure 4) and its coordinates are (I_Q, J_Q). L_i^ξ and L_j^η

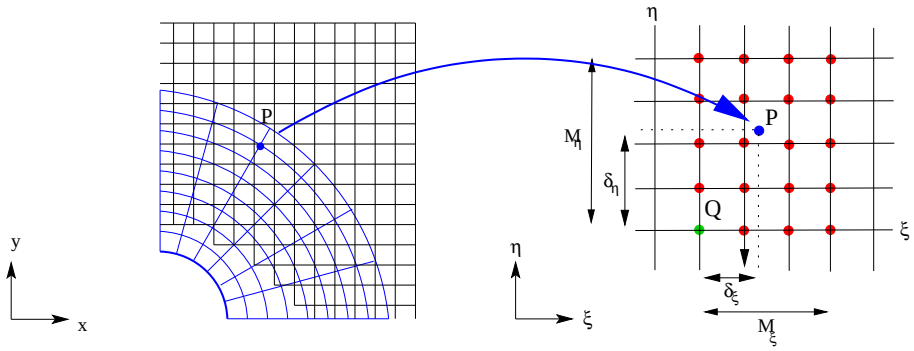

Figure 4. Example of a 2-D interpolation stencil: 2-D communication between a circular and a Cartesian component grids.

are the Lagrangian coefficients in the two directions defined as:

$$L_i^\xi = \prod_{m=0, m\neq i}^{M_\xi - 1} \frac{\delta_\xi - m}{i - m} \quad \text{and} \quad L_j^\eta = \prod_{m=0, m\neq j}^{M_\eta - 1} \frac{\delta_\eta - m}{j - m}$$

where δ_ξ and δ_η called the offsets are the coordinates of P, the receiver point, with respect to Q in the computational domain. For simplicity and isotropic reason, in the following, we have chosen $M_\xi = M_\eta = M$ which is also the Lagrangian polynomial order in the computational domain.

In addition, the SAFARI code is parallelized by domain decomposition on each component grid for application to massively-parallel platforms. The communication between each domain is performed via the MPI library.

C. Linear analysis

In 1-D, the Lagrangian interpolation procedure in Equation (14) can be rewritten as follows:

$$\phi(x_P) \approx \sum_{i=0}^{M-1} L_i \phi(x_Q + i\Delta x) \quad \text{with} \quad L_i = \prod_{m=0, m\neq i}^{M-1} \frac{\delta - m}{i - m} \tag{15}$$

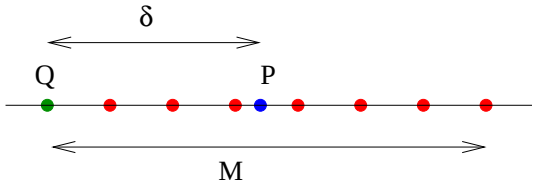

Figure 5. Example of a 1-D interpolation stencil.

with $x_P = x_Q + \delta\Delta x$. The interpolation error is now quantified using a one-dimensional Fourier error analysis following Sherer and Scott.[12] Thus, we consider a single harmonic: $\phi(x) = e^{Ikx}$ as previously in Section III with the wavenumber k and $I^2 = -1$. The interpolation error factor can be defined as:

$$\mathcal{H}_{\text{itp}} = \frac{e^{I\delta k\Delta x}}{\sum_{i=0}^{M-1} L_i e^{Iik\Delta x}}$$

For a centered Lagrangian interpolation, we have $\delta \approx (M-1)/2$. The local error is displayed in Figure 6. The

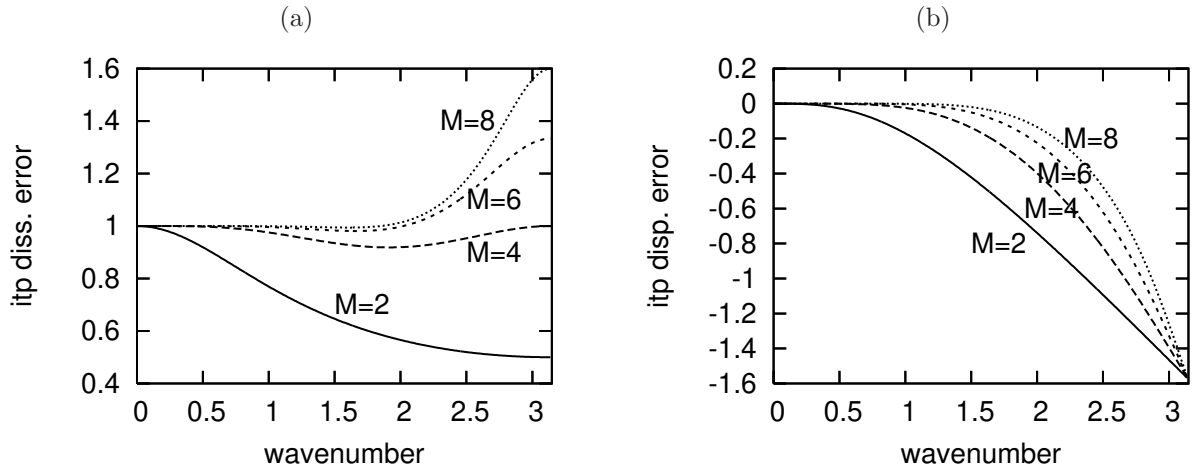

Figure 6. Local error of the interpolation process as a function of the wavenumber $k\Delta x$ with $M = 2, 4, 6$ and 8: (a) dissipation error or norm of $\mathcal{H}_{\text{itp}}$ and (b) dispersion error or phase of $\mathcal{H}_{\text{itp}}$.

Lagrangian interpolation procedure with $M = 2$ or $M = 4$ implies numerical errors in the wavenumber range not damped by the present algorithm according to the results in Section III. This can lead to the generation of spurious waves. In contrast, Lagrangian interpolation with $M = 6$ or $M = 8$ seems to be suitable with the present numerical algorithm. To compare quantitatively the different polynomial interpolation, the limit accuracy limit in Equation (10) is still used: $|1 - \mathcal{H}_{\text{itp}}| \leq 5 \times 10^{-4}$. The accuracy domains are given in the table 1. The range of wavenumber well resolved by the present algorithm is thus incorporated in the one of

M	$k_a\Delta x$	$\lambda_a/\Delta x$
2	0.04	169.81
4	0.34	18.48
6	0.65	9.59
8	0.90	6.94

Table 1. Accuracy limit of the Lagrangian polynomial interpolations with $M = 2, 4, 6$ and 8.

the Lagrangian polynomial interpolation with $M = 6$ and $M = 8$.

D. Boundary conditions

1. *Wall boundaries*

In order to preserve low-dissipation and low-dispersion properties near wall boundaries, 11-point non-centered finite-difference schemes in conjunction with explicit 11-point non-centered low-pass filter proposed by Berland *et al.*[31] are used. Theses two procedures are optimized in the wavenumber space to recover the bandwidth properties of the centered ones in Equations (4) and (7). However, the non-centered schemes suffer from numerical instability. Therefore, in the case of strong flow gradients near wall boundaries, explicit centered filtering of lower order can optionally be used to ensure this numerical stability.

2. *Non-reflecting boundary conditions*

Inlet and outlet boundary conditions are based on the Thompson's characteristic boundary conditions.[32] The conditions are supposed to locally be one-dimensional and inviscid. Then, the convective terms in the boundary-normal direction are split into several waves with different characteristic velocities. Finally, the unknown incoming waves are expressed as a function of known outgoing waves. The 3-D far-field radiation boundary conditions generalized by Bogey and Bailly[33] are applied on the boundaries to which only acoustic perturbations are reaching.

V. Canonical test problems

In this Section, several canonical problems are reported. These cases involve classical problems encountered in computational aeroacoustics (CAA) as well as in computational fluid dynamics (CFD).

A. Shock-capturing properties

The conservative and shock-capturing properties of the proposed algorithm are evaluated on classical 1-D shock tube and 2-D inviscid flow with discontinuities. The interaction shock/vortex is also retained to check that the non-linear procedure does not damage the bandwidth properties of the spatial discretization.

1. *One-dimensional shock tube*

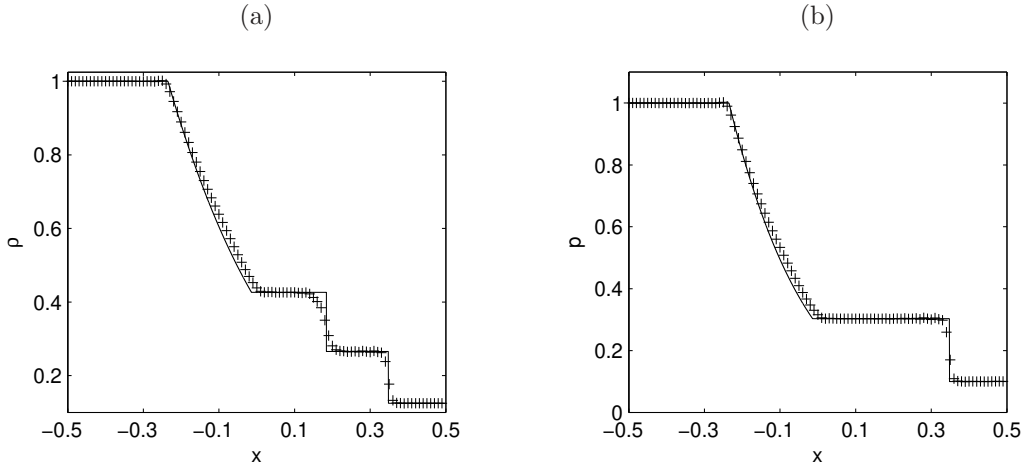

Figure 7. Comparison between analytical (-) and numerical (+) solutions for the Sod's shock tube with 100 cells: (a) density; (b) pressure.

First, the classical 1-D Sod's shock tube is considered: results are displayed in Figure 7 with $\mathsf{CFL} = 0.5$ and $\sigma_f = 0.2$. Only 100 cells ($\Delta x = 1/100$) are used for the computational domain $[-0.5; 0.5]$ as in Jiang and Shu.[34] The third shock wave is very well represented with a minimum of diffusion. The second contact discontinuity is well located by the algorithm with a diffusive character. Only the end of the first rarefaction

wave is not well located. On the pressure variable, small classical Gibbs oscillations are observed upstream the position of the shock wave.

2. Two-dimensional Mach 3 wind tunnel with a step

The second well-known test case is the Mach 3 wind tunnel with a step studied by Woodward and Colella.[35] The problem is initialized with a inviscid Mach 3 flow in the wind tunnel. Reflective boundary conditions are applied along the walls, whereas the inflow and outflow conditions are applied via the characteristics. No specific treatment is used for the singularity at the corner of the step. The grid resolution is the same as the

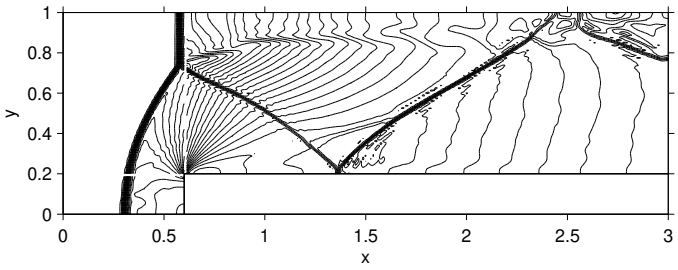

Figure 8. Inviscid 2-D Mach 3 flow past a step: density contour at $t = 4$.

one used by Woodward and Colella:[35] $N_\xi \times N_\eta = 240 \times 80$. Density contours with $\mathsf{CFL} = 0.8$ and $\sigma_f = 0.6$ are represented in Figure 8 exhibiting multiple shock reflections and interactions between different types of discontinuity. The locations of shocks are accurately represented. Kelvin-Helmholtz oscillations generated at the triple point are clearly visible. The generated waves propagate downstream and are refracted by the second and third reflected shocks. In addition, small Gibbs oscillations are observed due to the high-accuracy of the spatial scheme.

3. Two-dimensional shock/vortex interaction

This test case describes the interaction between a stationary shock and an inviscid vortex.[34] The compu-

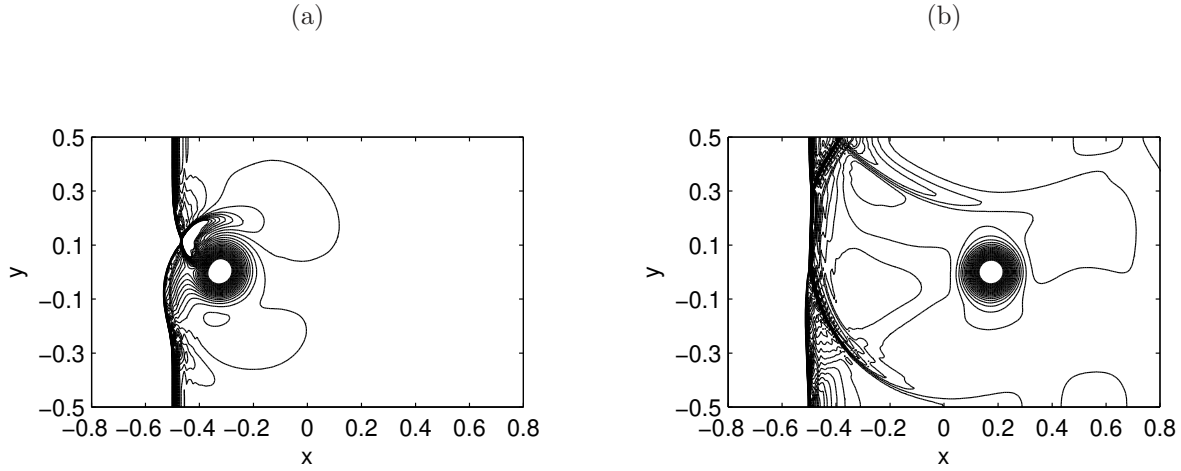

Figure 9. Inviscid vortex/shock interaction, pressure iso-contours: (a) thirty contours from 1.02 to 1.4 at $t = 0.35$ and (b) thirty contours from 1.1 to 1.3 at $t = 0.8$.

tational domain is taken to be $[-1, 1] \times [-0.5, 0.5]$. A stationary Mach 1.1 shock normal to the x axis is

located at $x_s = -0.5$. Its left side is $(\rho, u, v, p)_{\mathrm{L}} = (1, 1.1\sqrt{\gamma}, 0, 1)$ and its right side is obtained with the Rankine-Hugoniot relations. A vortex is superposed to the flow and centers at $(x_c, y_c) = (-0.75, 0)$. According to,[34] the vortex is described as a perturbation of the velocity (u, v), the entropy $S = \ln(p/\rho^\gamma)$ and the temperature $T = p/\rho$ of the base flow:

$$\begin{cases} \delta u &= \epsilon a e^{\alpha(1-a^2)}(y - y_c)/r \\ \delta v &= \epsilon a e^{\alpha(1-a^2)}(x_c - x)/r \\ \delta S &= 0 \\ \delta T &= (1-\gamma)\epsilon^2 e^{2\alpha(1-a^2)}/4\alpha\gamma \end{cases} \quad \text{with} \quad \begin{cases} a &= r/r_c \\ r &= \sqrt{(x-x_c)^2 + (y-y_c)^2} \\ r_c &= 0.05 \\ \epsilon &= 0.3 \\ \alpha &= 0.204 \end{cases}$$

The computation is performed with an uniform grid of 251×101 points and with $\mathsf{CFL} = 0.9$. The upper and lower boundaries are set to be reflective. The results plotted in Figure 9 are in good agreement with the one obtained in.[36] An accurate vortex/shock resolution is obtained.

B. Multi-domain approach

The use of overlapping regions can generate spurious acoustic waves as it has been observed by Desquesnes *et al.*[13] In the present paper, the influence of the polynomial order on the accuracy of the optimized finite-difference scheme and on the generation of spurious acoustic waves is characterized. Two numerical test cases are retained: the convection of an inviscid vortex through overset regions and the diffraction of a monopolar acoustic source by a cylinder.

1. *Two-dimensional advection of a vortex through interpolation zones*

The vortex is defined by the initial conditions using the following values:

$$\begin{cases} \rho &= 1 \\ u &= M_\infty + y\ \epsilon\ \exp\left(-\dfrac{\log(2)}{\alpha^2}(x^2+y^2)\right) \\ v &= x\ \epsilon\ \exp\left(-\dfrac{\log(2)}{\alpha^2}(x^2+y^2)\right) \\ p &= \dfrac{1}{\gamma} \end{cases}$$

where $M_\infty = 0.5$ is the free-stream Mach number, $\epsilon = 0.01$ is the vortex strength and $\alpha = 3\Delta x$ is the Gaussian half width. The computational domain composed by three uniform component grids connected by

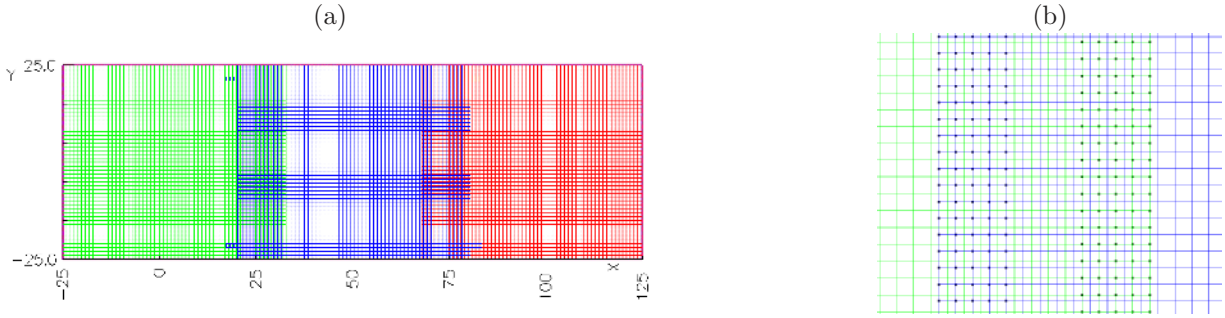

Figure 10. Overlapping grid: (a) general view; (b) detailed view of the center of an overlapping region ($y = 0$).

two overlapping regions, is displayed in Figure 10 (a). The left and the right grids contain $N_\xi \times N_\eta = 51 \times 51$ points. The centered grid consists of $N_\xi \times N_\eta = 51 \times 52$ and is shifted by half a grid size length in x-direction such as displayed in Figure 10 (b). This avoids interpolation points to coincide with grid points in the zone

of the vortex travel. The radiation boundary conditions are applied to all boundaries. Five simulations are done with varying interpolation order ranging from 2 to 10. For all computations, we fix CFL=0.25 to avoid numerical errors due to the time integration. The simulations are carried out for 800 iterations, that is the time required to convect the vortex over $100\Delta x$ and to ensure the transit through the two overlapping regions.

Figure 11 displays a sequence of the instantaneous pressure field when the vortex, characterized by a pressure minimum, meets the first overlapping region. Figures 11 (a), (b) and (c) are obtained using Lagrangian polynomial order $N_{\text{order}} = 2, 6$ and 10 respectively. The acoustic wave leaving the computational domain at the first and second instant is due to an adaptation of the pressure field to the velocity field at the beginning of the simulation. Using the second-order interpolation, strong acoustic disturbances are generated and contaminate the physical solution. Those parasite waves are significantly reduced when using sixth-order Lagrangian polynomials and disappear when a tenth-order interpolation scheme is used. This non-linear numerical example supports the linear analysis performed previously.

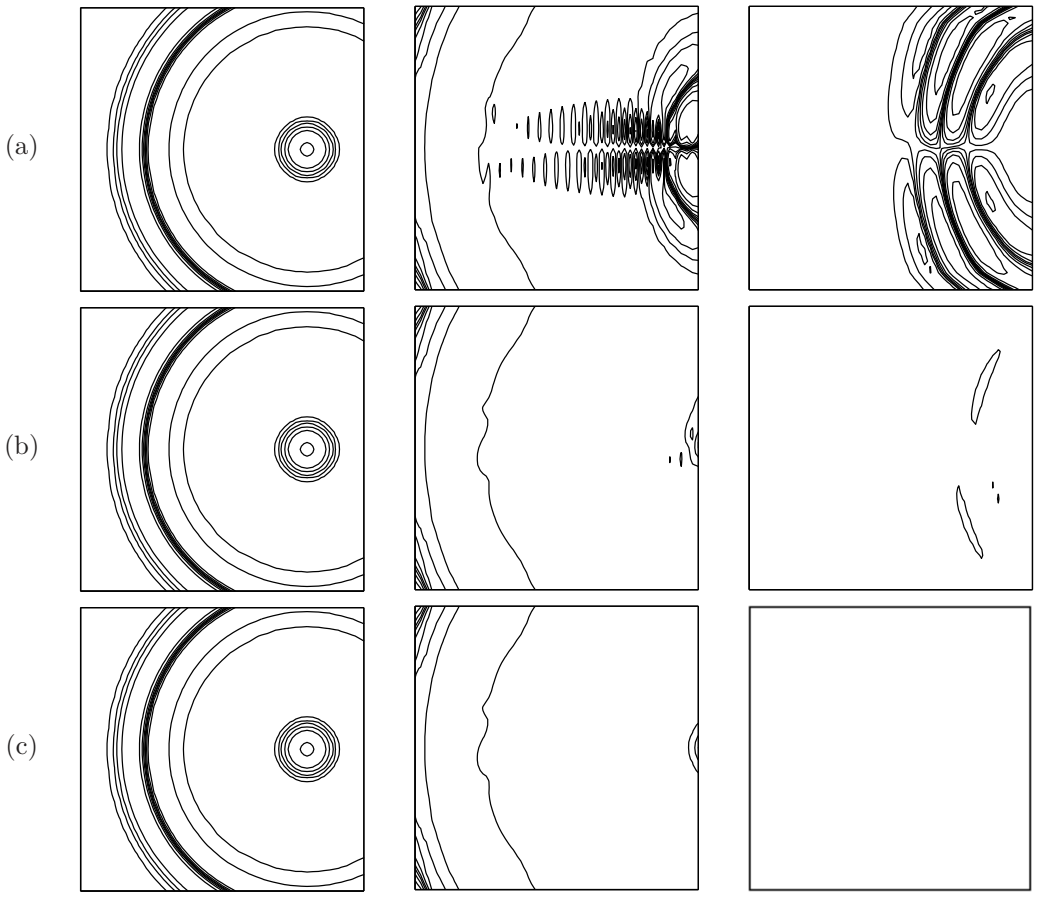

Figure 11. Iso-contours of the instantaneous pressure field computed in the left grid during the passage of the vortex through the overlapping region using Lagrangian polynomials of order: (a) $N_{\text{order}} = 2$; (b) $N_{\text{order}} = 6$ and (c) $N_{\text{order}} = 10$.

In order to quantify the generation of spurious acoustic perturbations, the time evolution of the L_2 norm of the residual pressure in the left grid has been computed:

$$R_p = \sqrt{\frac{1}{N_\xi N_\eta} \sum_{i,j}^{N_\xi, N_\eta} p'^2_{i,j}}.$$

This residual obtained with the overset-grid approach is compared to the reference single-block computation in Figure 12. The peak observed during the first 200 iterations for all setups is associated to the transitional

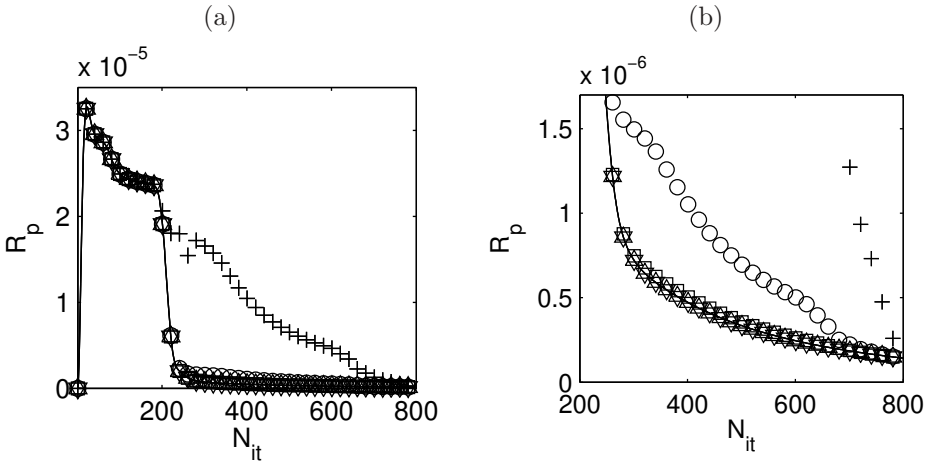

Figure 12. (a) Time evolution of the residual pressure R_p in the left grid. (b) Detailed view on the residual pressure; ——— R_p of the single-block computation (reference solution); solution obtained with overset grids using different interpolation orders: + $N_{\mathbf{order}} = 2$, ○ $N_{\mathbf{order}} = 4$, □ $N_{\mathbf{order}} = 6$, △ $N_{\mathbf{order}} = 8$, ▽ $N_{\mathbf{order}} = 10$.

pressure pulse. The decrease of the residual pressure, indicates that this pressure pulse leaves the computational domain without any spurious reflections. When the vortex hits the overlapping zone ($N_{\mathrm{it}} = 200$), the residual pressure obtained with second-order polynomials shows a significant increase and confirms the generation of acoustic waves observed in Figure 11 (a). Using fourth-order polynomials the reflections are only visible in a zoom on the last 600 iterations shown in Figure 12 (b). For orders higher than 6 the residual pressure evolves like in the single-block computation and the reflections are negligible.

Finally, to quantify the error on the aerodynamic field, the L_2 norm of the difference between the exact and the computational swirl velocity when the vortex has reached its final position at $x = 100\ \Delta x$ is considered. This error is computed along the x-axis at $y = 0$ such as:

$$L_v = \sqrt{\frac{1}{N_\xi} \sum_{i}^{N_\xi} v_i|^2_{y=0}}.$$

The L_v values normalized by the single-block result are plotted in Figure 13. It reveals that for polynomial

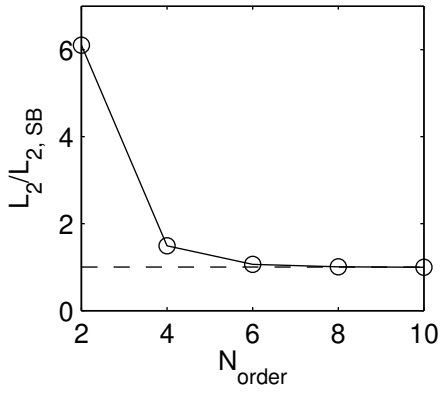

Figure 13. L_2 norm of the error of the swirl velocity normalized by the L_2 obtained for the computation on a single block.

orders higher than 6 the accuracy of the numerical algorithm is only governed by the spatial and time integration errors: the interpolation error becomes negligible. In order to reduce the effort in CPU and

storage, the order of polynomial interpolation is limited to eighth-order for 2-D problems and to sixth-order for 3-D problems in the present work.

2. 1-D shock tube with 2-D overlapping grids

The preservation of the present high-order algorithm via the overset-grid strategy for CFD problems has been discussed in the previous Section. However, as the interpolation procedure does not ensure the conservativity property of the global algorithm, it is necessary to evaluate the damage caused by this process on the computation by revisiting for instance the Sod's shock tube computed previously on a single block. Consider

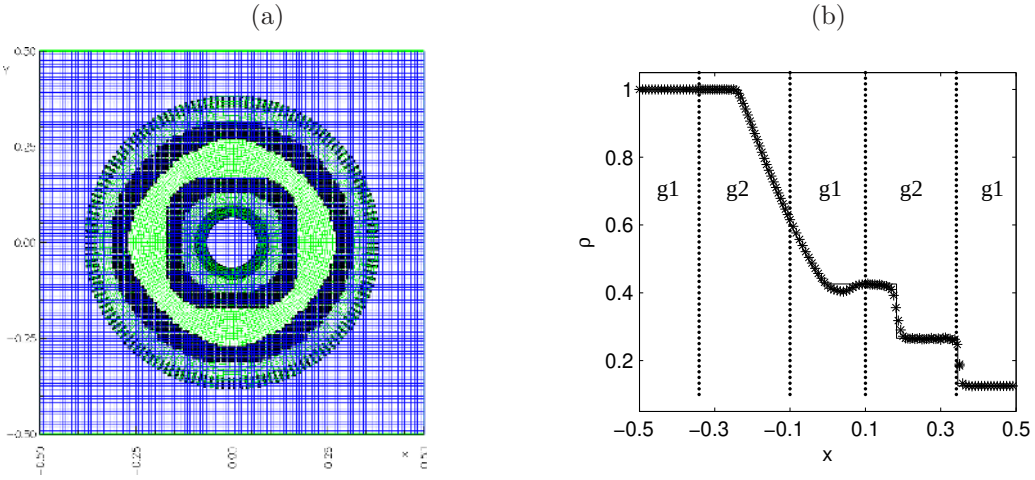

Figure 14. Computation of the Sod's shock-tube with overlapping grids: (a) general view of the computational domain with the two grids; (b) comparison between analytical (-) and numerical (*) density profiles at $y = 0$.

now the 2-D computational domain: $[-0.5; 0.5]\times[-0.5; 0.5]$, composed by two component grids: one Cartesian g1 with $\Delta x = \Delta y = 1/100$ and one circular g2 plotted in Figure 14 (a). Eighth-order Lagrangian polynomials are used for the communication between the two component grids. The computation is then performed with CFL=0.5 and $\sigma_f = 0.2$. According to Figure 14 (b), the numerical density profile at $y = 0$ is in good agreement with the analytical one except for the end of the first rarefaction wave where a spurious undershoot is present due to the passage of the second contact discontinuity through the overlapping-grid zone. However, the wave speeds are well retrieved even with the interpolation procedure. The vertical lines represent the limit between the two component grids.

3. Diffraction of monopolar acoustic source by a cylinder

This test case is issued from the second CAA workshop[37] and serves to check if sixth-order Lagrangian polynomials are sufficient to recover the accuracy of the high-order finite-difference scheme when only acoustic perturbations are involved. The numerical setup is represented in Figure 15. The 2-D Euler equations are solved in non-dimensional form. The reference length scale is the diameter of the cylinder d. A Gaussian shaped source is placed at $(x_s, y_s) = (4, 0)$:

$$S = \epsilon \sin(\omega t) \exp\left[\ln(2)\frac{(x - x_s)^2 + (y - y_s)^2}{b^2}\right],$$

where the angular frequency is given by $\omega = 8\pi$ and the Gaussian half-width by $b = 0.2$. Originally the test case proposes to solve the linearized Euler equations. For the non-linear Euler equations, a sufficiently small source strength ϵ has to be introduced, in order to avoid non-linear effects. In this work $\epsilon = 1 \times 10^{-6}$ has been chosen. For initial conditions air at rest at the pressure $p_0 = 1/\gamma$ and with the density $\rho_0 = 1$ is taken. The wave length associated to the source is $\lambda = c_0/4 = 0.25$. Note that the source is non compact since the wave length is of the same order as the source size.

A first simulation is done using a single cylindrical grid. The grid contains $N_r \times N_\theta = 781 \times 751 = 5.9 \times 10^5$ grid points which are spaced uniformly in r- and θ-direction. The number of points in the azimuthal direction

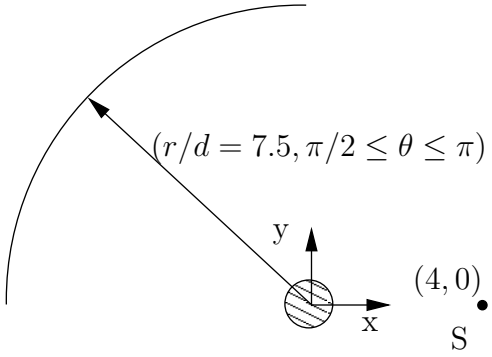

Figure 15. Configuration for the diffraction test cast: the time harmonic monopolar source is placed at point S. The directivity $D(\theta)$ will be measured on a arc at $r/d = 7.5$, $\pi/2 \leq \theta \leq \pi$.

N_θ is chosen to ensure a wave to be resolved by 7 points at $r/d = 7.5$. The number of points in radial direction N_r is taken to respect a ratio $\Delta r/\Delta\theta = 1.5$ at the cylinder wall. The directivity given by:

$$D(\theta, r) = r\frac{1}{T}\int^{T} p'(\theta, r)^2 \, \mathrm{d}t$$

is computed on a arc with $r/d = 7.5$ and $\pi/2 \leq \theta \leq \pi$ and is compared to the analytical solution of the problem. The computed curve and the analytical curve compare well in Figure 16.

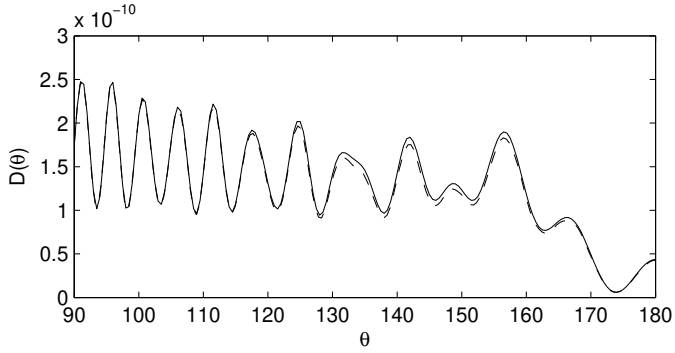

Figure 16. Directivity $D(\theta) = r < p'^2 >$ at $r/d = 7.5$: ——— computed solution; − − − analytical solution.

Figure 17 (a) shows the simulated fluctuating pressure field. The acoustic waves coming from the non-compact source generate a diffraction field. A silent zone behind the cylinder can be observed.

In a second simulation the same test case is performed using the overset-grid approach. The overset grid is composed of 2 grids: one cylindrical grid and one uniform grid. The uniform grid is generated to resolve acoustic wave with 7 points per wave length $\Delta x = \Delta y = \lambda/7 = 1/28$. The uniform grid is extended $-10 \leq x, y \leq 10$. The cylindrical grid is spaced uniformly in azimuthal and radial direction and is limited by the outer radius $r_a/d = 1.5$. In the radial direction the grid length is chosen to be $\lambda/13$ and the number of grid points in azimuthal direction is taken to ensure that the aspect ratio of the radial and azimuthal grid spacing is $\Delta r/\Delta\theta \approx 1.1$. The overset grid contains 3.2×10^5 grid points, 45% less grid points than used for the single-block computation.

Figure 17 (b) shows the fluctuating pressure field for the overset grid using sixth-order interpolation polynomials. Even in the cylinder near region, the diffracted field is very similar to the reference single-block computation. The acoustic waves propagate through the overlapping region without generating spurious reflections. In Figure 18, the quantity $D(\theta, r)$ along a line defined by $\theta = \pi/2$ and $0.5 \leq r/d \leq 10$ is compared with the analytical solution for the interpolation order of 2 and 6. Use of second-order polynomials leads to large discrepancies in the near cylinder region. For higher orders than six, the error made by the interpolation procedure tends to zero.

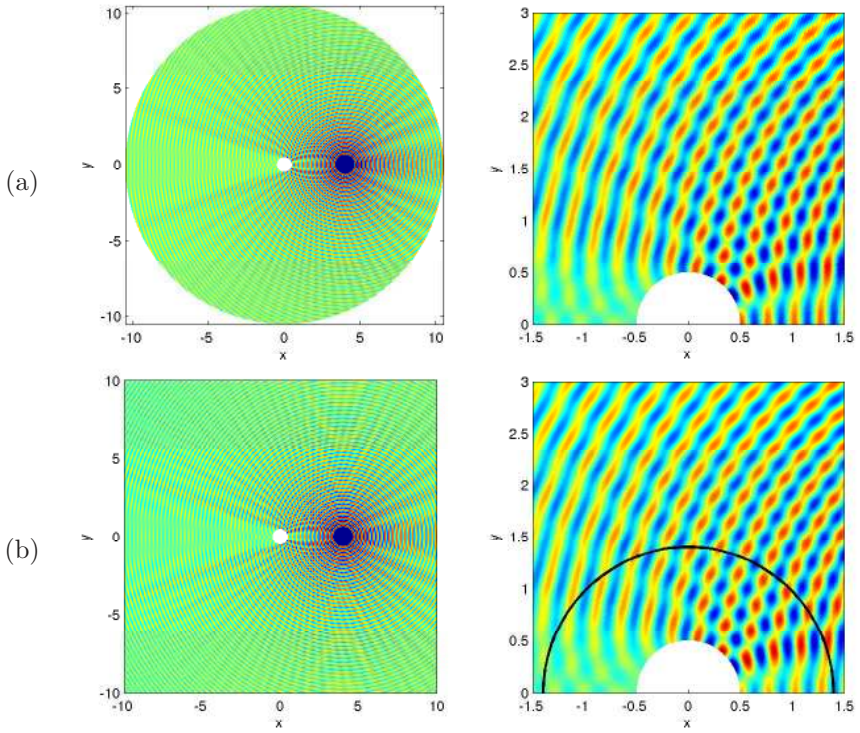

Figure 17. Diffraction of a non-compact source by a cylinder: fluctuating pressure field (color scales $\leq 10^{-10}$ Pa): (a) obtained by the single-block computation; (b) obtained using overset-grid approach and sixth-order interpolation polynomials. The solid line stands for the boundary of the cylindrical grid.

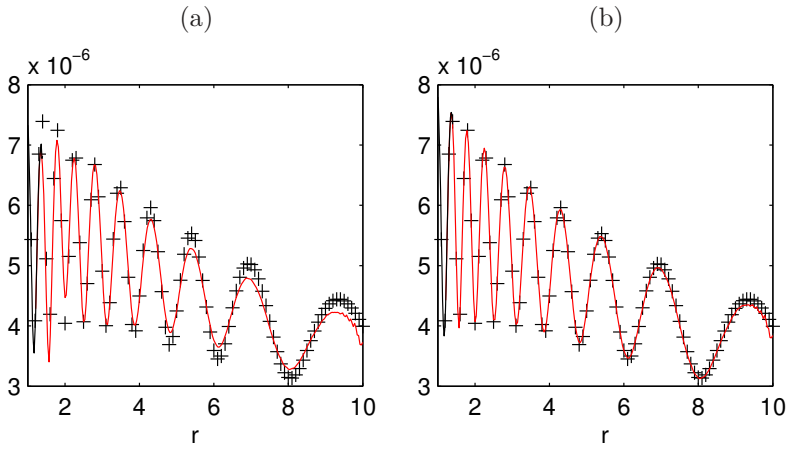

Figure 18. Directivity $D(\theta, r)$ at $0.5 \leq r/d \leq 10$ and $\theta = \pi/2$ for different order of interpolation: (a) second-order (b) sixth-order; —— computed solution; + analytical solution.

In this Section, the overset-grid approach has been successfully applied and the results compare very well with the analytical solution. The test case reveals that sixth-order Lagrangian polynomials are sufficient when acoustic perturbations are involved in order to maintain the global accuracy of the 11-point finite-difference scheme.

VI. Application on moving grids

For the application of the algorithm for moving/deforming grids, the approach retained in this paper to compute the time metrics in order to provide metric cancellation and free-stream preservation is based on the one proposed by Visbal and Gaitonde.[18] The time derivative in Equation (1) is split into two parts and the second term is evaluated using the GCL condition. And, finally, the following equation is solved with the high-order algorithm presented in Section III:

$$\partial_\tau U + \underbrace{J\left\{\partial_\xi E + \partial_\eta F + \partial_\zeta G - U\left[\partial_\xi\Big(\frac{\xi_t}{J}\Big) + \partial_\eta\Big(\frac{\eta_t}{J}\Big) + \partial_\zeta\Big(\frac{\zeta_t}{J}\Big)\right]\right\}}_{\mathcal{R}} = 0 \tag{16}$$

The time metrics are evaluated using the grid velocity $\vec{V}_e = (x_\tau, y_\tau, z_\tau)^T$ via the following relations:

$$\left\{\begin{array}{rcl} \dfrac{\xi_t}{J} & = & -\Big(x_\tau\dfrac{\xi_x}{J} + y_\tau\dfrac{\xi_y}{J} + z_\tau\dfrac{\xi_z}{J}\Big) \\ \dfrac{\eta_t}{J} & = & -\Big(x_\tau\dfrac{\eta_x}{J} + y_\tau\dfrac{\eta_y}{J} + z_\tau\dfrac{\eta_z}{J}\Big) \\ \dfrac{\zeta_t}{J} & = & -\Big(x_\tau\dfrac{\zeta_x}{J} + y_\tau\dfrac{\zeta_y}{J} + z_\tau\dfrac{\zeta_z}{J}\Big) \end{array}\right. \tag{17}$$

These relations are similar to the classical ALE (Arbitrary Lagrangian Eulerian) expression in a finite-volume framework. The spatial derivative in Equation (16) are approximated by the spatial scheme in Equation (4) and the time integration is performed with RK4 yielding:

$$U^{(l)}_{i,j,k} = U^n_{i,j,k} - \Delta\tau\beta^{(l)}\mathcal{R}^{(l-1)}_{i,j,k} \quad \forall l \in \{1, ..., 4\} \tag{18}$$

with $U^{(0)} = U^n$ and $\mathcal{R}_{i,j,k}$ the discretization of the residual $\mathcal{R}$. The Courant-Friedrich-Lewy number in the ξ-direction is defined by:

$$\mathsf{CFL}_\xi = \frac{\Delta t\left(|\xi_t + \Theta_\xi| + c||\vec{\nabla}\xi||\right)}{\Delta\xi} \tag{19}$$

and the numerical stability requires to satisfy the following relation:

$$\mathsf{CFL} = \max(\mathsf{CFL}_\xi, \mathsf{CFL}_\eta, \mathsf{CFL}_\zeta) \leq 1$$

In the same way, the mesh displacement is linked to a new stability requirement. In order to introduce this new stability constraint, a 1-D model is considered. In the physical space, the time and spatial variables are independent which is equivalent to a non-linear advection equation in the computational domain using the chain-derivative rules:

$$\frac{\mathrm{d}x}{\mathrm{d}t} = 0 \iff \partial_\tau x + \xi_t\partial_\xi x = 0$$

For this equation, the stability constraint is based on the ratio $C_\xi = \dfrac{|\xi_t|\Delta\tau}{\Delta\xi}$. According to Equations (17) and (19), it follows that:

$$\frac{|d_\xi|}{\Delta\xi}||\vec{\nabla}\xi|| < \mathsf{CFL}_\xi \tag{20}$$

where $d_\xi = \vec{V}_e.\vec{\nabla}\xi/||\vec{\nabla}\xi||$ is the displacement in the ξ-direction. Thus, the mesh displacement is limited and the maximal allowed value is driven by the CFL value linked by the updating of the flow variables.

In order to ensure the synchronization between the flow variables and the grid coordinates, the RK4 scheme is also used for the updating of the grid coordinates:

$$\left\{\begin{array}{lcl} x_{i,j,k}^{(l)} & = & x_{i,j,k}^{n} + \Delta\tau\beta^{(l)}(x_\tau)_{i,j,k}^{(l-1)} \\ y_{i,j,k}^{(l)} & = & y_{i,j,k}^{n} + \Delta\tau\beta^{(l)}(y_\tau)_{i,j,k}^{(l-1)} \\ z_{i,j,k}^{(l)} & = & z_{i,j,k}^{n} + \Delta\tau\beta^{(l)}(z_\tau)_{i,j,k}^{(l-1)} \end{array}\right. \tag{21}$$

for $l \in \{1,..,4\}$ and with $x^{(0)} = x^n$, $y^{(0)} = y^n$, and $z^{(0)} = z^n$.

As the relative position of the overlapping grids changes continuously during the flow simulation, the interpolation data used for the communications between the component grids must be updated at each stage of the RK4 scheme. In practice, this updating is performed via the overlapping grid generator *Ogen*.[30] The validation procedure of the application of our high-order algorithm on dynamic meshes is performed in two stages. The first one concerns single-block computations in order to validate the calculation of the time metrics and the grid coordinate updating. Then, multi-block computations is used to couple the updating of the interpolation data with the numerical algorithm.

A. Inviscid vortex advection

The first validation test case is the vortex advection on a dynamically deforming 2-D mesh. The computational domain is taken as $[-2,2]\times[-1,1]$. Initially, an uniform mesh is retained with $\Delta x_0 = \Delta y_0 = 1/100$. The grid speed is analytically specified by the following equations:

$$\left\{\begin{array}{lcl} (x_\tau)_{i,j} & = & 2\pi\omega A_x \Delta x_0 \cos(2\pi\omega t)\sin\left(n_x\pi\dfrac{y_{i,j}(0)-y_{\min}}{y_{\max}-y_{\min}}\right)\alpha_x \\ (y_\tau)_{i,j} & = & 2\pi\omega A_y \Delta y_0 \cos(2\pi\omega t)\sin\left(n_y\pi\dfrac{x_{i,j}(0)-x_{\min}}{x_{\max}-x_{\min}}\right)\alpha_y \end{array}\right. \tag{22}$$

with

$$\begin{array}{lcl} \alpha_x & = & \exp\left(-4\log(2)\dfrac{x_{i,j}(0)^2+y_{i,j}(0)^2}{(x_{\max}-x_{\min})^2}\right) \\ \alpha_y & = & \exp\left(-4\log(2)\dfrac{x_{i,j}(0)^2+y_{i,j}(0)^2}{(y_{\max}-y_{\min})^2}\right) \end{array}$$

The grid coordinates are then provided via the RK4 scheme with the assumption that the grid speed is constant during a time step:

$$\left\{\begin{array}{lcl} x_{i,j}^{(l)} & = & x_{i,j}^{n} + \Delta\tau\beta^{(l)}(x_\tau)_{i,j}^{n} \\ y_{i,j}^{(l)} & = & y_{i,j}^{n} + \Delta\tau\beta^{(l)}(y_\tau)_{i,j}^{n} \end{array}\right. \qquad \forall l \in \{1,..,4\}$$

In fact, only the domain $[x_{\min}, x_{\max}]\times[y_{\min}, y_{\max}]$ is dynamically deformed. The different parameters are: $A_x = A_y = 2$, $n_x = n_y = 6$, $x_{\min} = y_{\min} = -0.5$, $x_{\max} = y_{\max} = 0.5$ and $\omega = 2$.

Two computations are performed: one on a static grid, the initial uniform grid, and the other with the grid velocity expressed in Equation (22). These two computations are performed with $\mathsf{CFL} = 0.5$ designed with the initial non deformed grid in order to underline the effect of the mesh dynamic deformation on the high-order discretizations performance. The vortex is initially placed on $(x_c, y_c) = (0,0)$ and results given in this section are visualized when the vortex returns at its initial position. Comparison is given in Figures 19 and 20. The velocity fields in the static and deforming cases are similar which makes it possible to preserve the high-order schemes propagation properties on dynamically deforming meshes. The profile of the swirl velocity on $y = 0$ in Figure 20 shows the excellent agreement between the two computations. In addition, the dynamic deformation of the mesh implies a kind of numerical dissipation in the spatial high-order discretization characterized by a damping in the profile amplitude as in Visbal and Gaitonde.[18]

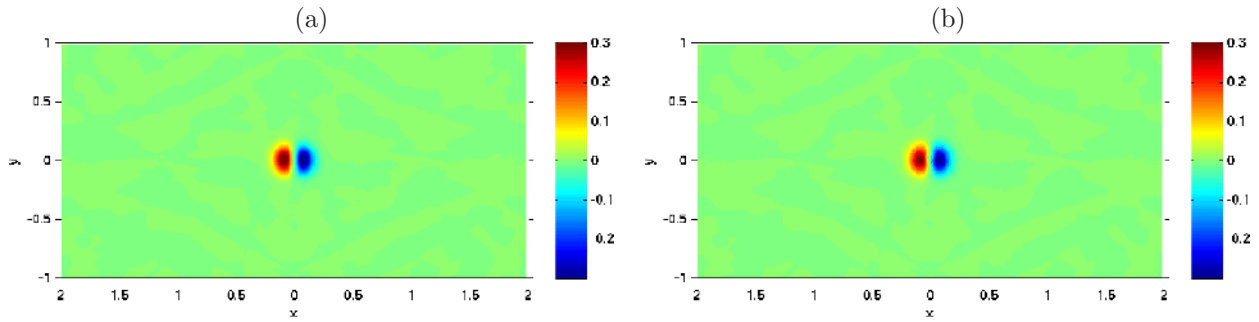

Figure 19. Comparison of the swirl velocity field: (a) in the static case ; (b) in the deforming case.

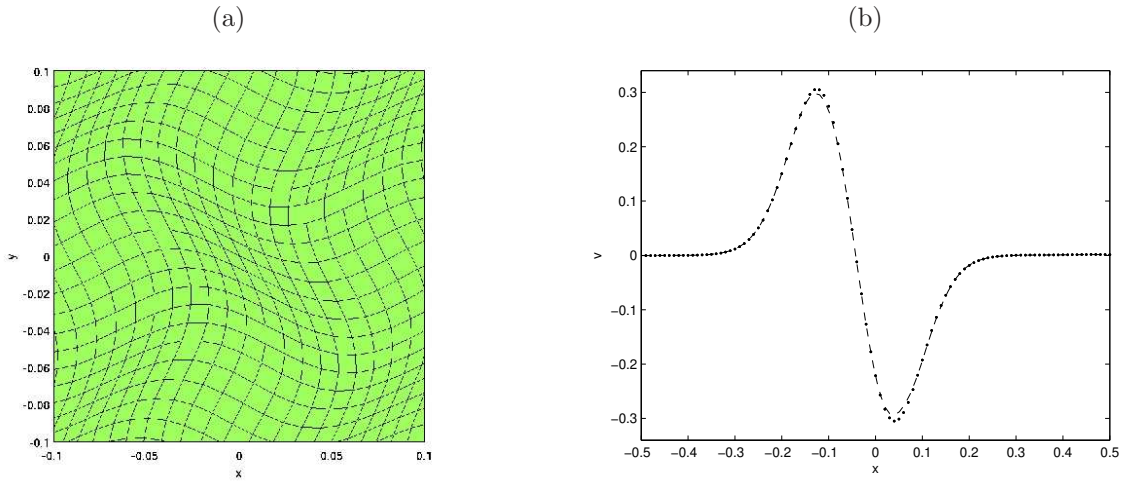

Figure 20. (a) Snapshot the grid deformation; (b) effect of the mesh dynamic deformation on the swirl velocity: . static case ; - - deforming case.

B. Cylinder advection in an inviscid uniform flow

The advection of a cylinder in a uniform flow at rest is now considered. The computational domain taken as $[-2,2]\times[-2,2]$ is divided in two grids. A cylindrical body-fitted grid moves with respect to a fixed Cartesian uniform grid with $\Delta x = \Delta y = 1/50$. The overlapping meshes are plotted in Figure 21. Initially, the center of the cylinder is located at $x_c = 0.85$.

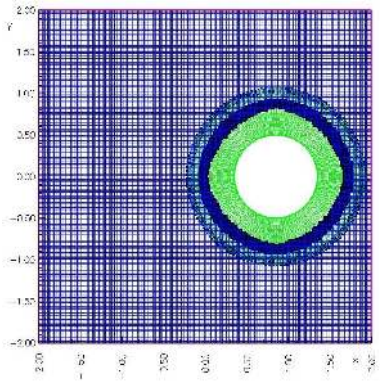

Figure 21. General view of the computational domain for the cylinder advection.

At every time step, a constant displacement of the cylindrical domain in the x-direction is imposed: $d_x = -0.08\Delta x$. Then, the mesh velocity is computed using the relation $x^{(l+1)} - x^{(l)} = d_x/4$ for every stage of the RK4 scheme. The computation is performed with $\mathsf{CFL} = 0.5$. Thus, the cylinder is shifted at the Mach number $M_e \approx 0.3$. The radiation boundary conditions are applied to all the boundaries of the fixed Cartesian domain. Then, at the wall, a no-slip condition is used following the displacement of the cylinder.

The velocity field of the inviscid flow over an moving cylinder is plotted in Figure 22 for three different positions. First, a transient acoustic wave is generated by the initial motion of the cylinder. Then, the wave leaves the computational domain and a symmetric stationary solution with respect to the cylinder is reached.

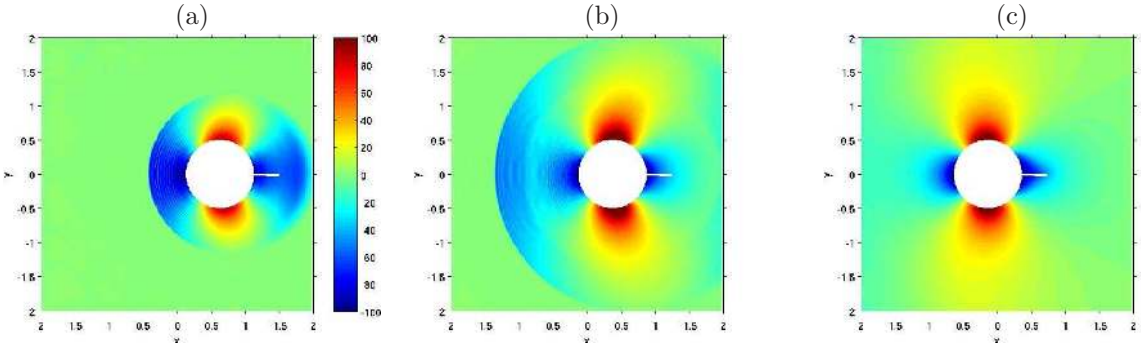

Figure 22. Time evolution of the streamwise velocity around the cylinder.

VII. 3-D complex applications

Two flow problems of industrial relevance are presented to show the ability of the algorithm to treat complex physical patterns in more realistic geometries.

A. Ducted cavity flow

The LES of the flow over a ducted cavity is performed with the proposed algorithm, see Figure 23. This configuration is characterized by a coupling between the self-sustained cavity oscillations and the transverse

acoustic duct mode. For example, at Mach number $M_\infty = 0.20$, the second cavity mode is coupled with the first pipe mode. The coupling phenomena is well reproduced numerically. More details concerning the computational issues and the physical analysis are given in.[38,39]

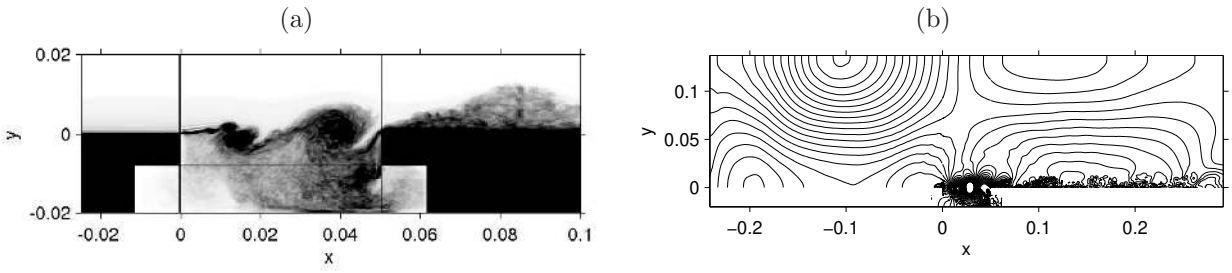

Figure 23. Ducted cavity flow for $M_\infty = 0.20$: (a) spanwise average of the vorticity modulus ; (b) pressure fluctuation in the duct

B. Sudden expansion

The LES of a transonic flow passing a sudden expansion in a duct is presented, see Figure 24. In this problem, strong interactions between shock oscillations internal, aerodynamic noise and acoustic duct modes are present. The validation of the numerical results via the comparison with experimental results is shown in details in.[40]

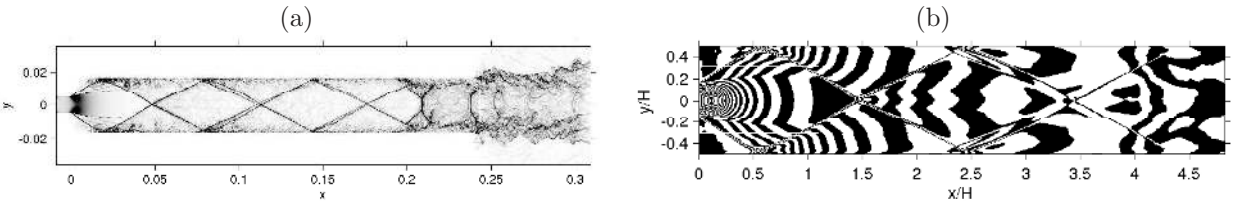

Figure 24. Sudden expansion of a transonic flow for pressure ratio $\tau = 0.15$: (a) instantaneous numerical Schlieren $||\nabla\rho||$; (b) iso-contours of the mean density

VIII. Conclusion and future works

A numerical method has been described for performing compressible LES in CAA applications. The scheme is based on a 11-point explicit optimized finite-difference algorithm in conjunction with a 11-point optimized spatial low-pass filter. A non-linear filter is implemented to capture discontinuities in compressible flows. This filter is based on a modified Jameson sensor to detect the location of shock waves. In order to address complex geometrical configurations, overlapping grids are used and the communications between domains are performed via high-order Lagrangian interpolation. The validation procedure has shown the ability of the algorithm to capture discontinuities without damaging its spectral behavior. The high-order overset-grid technique has proved to maintain the algorithm accuracy on both classical CFD and CAA applications even for moving grid applications. For compressible flows with complex physical interactions, the LES using the present algorithm well predicts the flow/acoustics coupling and the turbulence/shock interactions. Thus, the present scheme appears to provide a robust and accurate tool for performing LES of realistic compressible flows for CAA applications.

A more detailed validation procedure is in progress to check the accuracy of the present algorithm for moving grids. To address fluid/structure interaction, the coupling between flow patterns and structure dynamics will be studied with the aim of preserving the high-order accuracy of the present solver. The choice of the time integration method is also to be considered. In the explicit method used in this work, the

time step is imposed by stability constraints. However, the time step needed to respect the physical time scales of the turbulent flow may be larger. This is the case for turbulent wall-bounded flows, for example. The use of implicit time integration method would make it possible to circumvent the numerical stability by using a time step only driven by the flow physics.[21,41]

Acknowledgments

This work is supported by the "Agence Nationale de la Recherche" under the reference ANR-06-CIS6-011. The authors want to thank Dr. Bill Henshaw for his useful advice concerning the overset strategy.

A. 11-point scheme and filter coefficients

s_0	0.0	d_0	0.2150448841109084
s_1	0.872756993962667	d_1	−0.1877728835894673
s_2	−0.286511173973333	d_2	0.1237559487873421
s_3	0.090320001280000	d_3	−0.0592275755757438
s_4	−0.020779405824000	d_4	0.0187216091572037
s_5	0.002484594688000	d_5	−0.0029995408347887

Table 2. Scheme and filter coefficients proposed by Bogey and Bailly[10]

B. Finite-volume formulation of the 11-point scheme

In a similar way as Popescu *et al.*,[42] a finite-difference scheme can be recasted in a finite-volume framework. We consider the following non-linear conservation law:

$$\partial_t u + \partial_x f(u) = 0. \tag{23}$$

A finite-difference scheme can be written in the classical form:

$$\partial_x f(u)|_i \approx \frac{1}{\Delta x} \sum_{m=-r}^{q} s_m f(u_{i+m}).$$

On the other hand, a finite-volume discretization leads to:

$$\frac{\mathrm{d}}{\mathrm{d}t} \int_{x_{i-1/2}}^{x_{i+1/2}} u(x,t)\mathrm{d}x + f_{i+1/2} - f_{i-1/2} = 0.$$

Thus, a finite-volume formulation of the finite-difference scheme is:

$$\sum_{m=-r}^{q} s_m f(u_{i+m}) = f_{i+1/2} - f_{i-1/2},$$

with

$$f_{i+1/2} = \sum_{m=-r+1}^{q} \beta_m f(u_{i+m}).$$

Finally, the finite-volume coefficient β_m can be expressed using the finite-difference ones:

$$\left\{ \begin{array}{rcll} \beta_q & = & s_q & \\ \beta_m - \beta_{m+1} & = & s_m & -r+1 \leq m \leq q-1 \end{array} \right.$$

Thus:

$$\beta_m = \sum_{j=m}^{q} s_j \tag{24}$$

for $-r+1 \leq m \leq q$

References

[1]Colonius, T. and Lele, S. K., "Computational aeroacoustics: progress on nonlinear problems on sound generation," *Prog. Aerospace Sci.*, Vol. 40, 2004, pp. 345–416.

[2]Bailly, C., Bogey, C., and Marsden, O., "Advances in computational aeroacoustics: challenges and issues," *7th International ERCOFTAC Symposium on Engineering Turbulence Modelling and Measurements (ETMM7), Limassol, Chyprus, 4-6 June,*, 2008, pp. 1–10.

[3]Colonius, T., Lele, S. K., and Moin, P., "Sound generation in a mixing layer," *J. Fluid Mech.*, Vol. 330, 1997, pp. 375–409.

[4]Freund, J. B., "Noise sources in a low-Reynolds-number turbulent jet at Mach 0.9," *J. Fluid Mech.*, Vol. 438, 2001, pp. 277–305.

[5]Gloerfelt, X., Bailly, C., and Juvé, D., "Direct computation of the noise radiated by a subsonic cavity flow and application of integral methods," *J. Sound Vib.*, Vol. 266, No. 1, 2003, pp. 119–146.

[6]Bodony, D. J. and Lele, S. K., "On using large-eddy simulation for the prediction of noise from cold and heated turbulent jets," *Phys. of Fluids*, Vol. 17, 2005.

[7]Bogey, C. and Bailly, C., "Large eddy simulations of transitional round jets: influence of the Reynolds number on flow development and energy dissipation," *Phys. of Fluids*, Vol. 213, No. 2, 2006, pp. 777–802.

[8]Bogey, C. and Bailly, C., "An analysis of the correlations between the turbulent flow and the sound pressure fields of subsonic jets," *J. Fluid Mech.*, Vol. 583, 2007, pp. 71–97.

[9]Tam, C. K. W. and Webb, J. C., "Dispersion-Relation-Preserving Finite Differences Schemes for Computational Acoustics," *J. Comp. Phys.*, Vol. 107, No. 2, 1993, pp. 262–281.

[10]Bogey, C. and Bailly, C., "A family of low dispersive and low dissipative explicit schemes for flow and noise computations," *J. Comp. Phys.*, Vol. 194, No. 1, 2004, pp. 194–214.

[11]Delfs, J. W., "An overlapped grid technique for high resolution CAA schemes for complex geometries," *AIAA Paper 2001-2199*, 2001.

[12]Sherer, S. E. and Scott, J. N., "High-order compact finite-difference methods on general overset grids," *J. Comp. Phys.*, Vol. 210, No. 2, 2005, pp. 459–496.

[13]Desquesnes, G., Terracol, M., Manoha, E., and Sagaut, P., "On the use of a high order overlapping grid method for coupling in CFD/CAA," *J. Comp. Phys.*, Vol. 220, No. 1, 2006, pp. 355–382.

[14]Viviand, H., "Formes conservatives des équations de la dynamique des gaz," *La Recherche Aérospatiale*, Vol. 158, 1974, pp. 65–66.

[15]Vinokur, M., "Conservation equations of gasdynamics in curvilinear coordinate systems," *J. Comp. Phys.*, Vol. 14, No. 105, 1974, pp. 48–56.

[16]Marsden, O., Bogey, C., and Bailly, C., "High-order curvilinear simulations of flows around non-Cartesian bodies," *J. Comput. Acoust.*, Vol. 13, No. 4, 2005, pp. 731–748.

[17]Suh, J., Frankel, S. H., Mongeau, L., and Plesniak, M. W., "Compressible large eddy simulation of wall-bounded turbulent flows using a semi-implicit numerical scheme for low Mach number aeroacoustics," *J. Comp. Phys.*, Vol. 215, No. 2, 2006, pp. 526–551.

[18]Visbal, M. R. and Gaitonde, D. V., "On the Use of Higher-Order Finite-Difference Schemes on Curvilinear and Deforming Meshes," *J. Comp. Phys.*, Vol. 181, No. 1, 2002, pp. 155–185.

[19]Thomas, P. D. and Lombard, C. K., "Geometric conservation law and its application to flow computations on moving grids," *AIAA J.*, Vol. 17, No. 10, 1979, pp. 1030–.

[20]Hirsch, C., *Numerical computation of internal and external flows*, J. Wiley and Sons, New-York, 1988.

[21]Rizzetta, D. P., Visbal, M. R., and Blaisdell, G. A., "A time-implicit high-order compact differencing and filtering scheme for large-eddy simulation," *Int. J. Numer. Methods Fluids*, Vol. 42, 2003, pp. 665–693.

[22]Vreman, A. W., Geurts, B. J., and Kuerten, J. G., "A priori tests of large-eddy simulation of compressible plane mixing layer," *J. Eng. Math.*, Vol. 118, No. 1, 1995, pp. 24–37.

[23]Emmert, T., *Development of a multidomain high-order algorithm for computational aeroacoustics. Application to subsonic and transonic confined flows*, Ph.D. thesis, École Centrale de Lyon, 2007.

[24]Kim, J. W. and Lee, D. J., "Adaptive Nonlinear Artificial Dissipation Model for Computational Aeroacoustics," *AIAA J.*, Vol. 39, No. 5, 2001, pp. 810–818.

[25]Moase, W. H., Brear, M. J., and Manzie, C., "The forced response of choked nozzles and supersonic diffusers," *J. Fluid Mech.*, Vol. 585, 2007, pp. 281–304.

[26]Yee, H. C., Sandham, N. D., and Djomehri, M. J., "Low-Dissipative High-Order Shock Capturing Methods Using Characteristic-Based Filters," *J. Comp. Phys.*, Vol. 150, No. 1, 1999, pp. 199–238.

[27]Jameson, A., Schmidt, W., and Turkel, E., "Numerical Solutions of the Euler Equations by Finite Volume Methods Using Runge-Kutta Time-Stepping Schemes," *AIAA Paper 81-1259*, 1981.

[28]Garnier, E., Mossi, M., Sagaut, P., Comte, P., and Deville, M., "On the use of the shock-capturing schemes for Large-Eddy Simulation," *J. Comp. Phys.*, Vol. 153, No. 2, 1999, pp. 273–311.

[29]Ducros, F., Ferrand, V., Nicoud, F., Weber, C., Darracq, D., Gacherieu, C., and Poinsot, T., "Large-Eddy Simulation of the Shock/Turbulence Interaction," *J. Comp. Phys.*, Vol. 152, No. 2, 1999, pp. 517–549.

[30]Henshaw, W. D., "Ogen : An Overlapping Grid Generator for Overture," Tech. Rep. UCRL-MA-132237, Lawrence Livermore National Laboratory, 1998.

[31]Berland, J., Bogey, C., Marsden, O., and Bailly, C., "High-order, low dispersive and low dissipative explicit schemes for multiple-scale and boundary problems," *J. Comp. Phys.*, Vol. 224, No. 2, 2007, pp. 637–662.

[32]Thompson, K. W., "Time-dependent boundary conditions for hyperbolic systems, II," *J. Comp. Phys.*, Vol. 89, No. 2, 1990, pp. 439–461.

[33]Bogey, C. and Bailly, C., "Three-dimensional non-reflective boundary conditions for acoustic simulations: far field formulation and validation test cases," *Acta Acustica*, Vol. 88, No. 4, 2002, pp. 463–471.

[34]Jiang, G.-S. and Shu, C.-W., "Efficient Implementation of Weighted ENO Schemes," *J. Comp. Phys.*, Vol. 126, No. 1, 1996, pp. 202–228.

[35]Woodward, P. R. and Colella, P., "The numerical simulation of two-dimensional fluid flow with strong shocks," *J. Comp. Phys.*, Vol. 54, No. 1, 1984, pp. 115–173.

[36]Zhou, Q., Yao, Z., He, F., and Shen, M. Y., "A new family of high-order compact upwind difference schemes with good spectral resolution," *J. Comp. Phys.*, Vol. 227, No. 1, 2006, pp. 1306–1339.

[37]Tam, C. K. W. and Hardin, J. C., editors, *Second Computational Aeracoutics (CAA) Workshop on Benchmark Problems*. NASA CP-3352, 1997.

[38]Emmert, T., Lafon, P., and Bailly, C., "Numerical Simulation of the Flow over a Confined Shallow Cavity," *Turbulence and Shear Flow Phenomena 5*, 2007.

[39]Emmert, T., Lafon, P., and Bailly, C., "Numerical study of aeroacoustic coupling in a subsonic confined cavity," *14th AIAA/CEAS Aeroacoustics Conference, Vancouver, Canada*, 2008.

[40]Emmert, T., Lafon, P., and Bailly, C., "Computation of Aeroacoustic Phenomena in Subsonic and Transonic Ducted Flows," *AIAA Paper 2007-3429*, 2007.

[41]Daude, F., Mary, I., and Comte, P., "Implicit time integration method for LES of complex flows," *Direct and Large-Eddy Simulation VI*, Springer, 2006, pp. 771–778.

[42]Popescu, M., Shyy, W., and Garbey, M., "Finite volume treatment of dispersion-relation-preserving and optimized prefactored compact schemes for wave propagation," *J. Comp. Phys.*, Vol. 210, No. 2, 2005, pp. 705–729.